Research Square

Preprints are preliminary reports that have not undergone peer review.
They should not be considered conclusive, used to inform clinical practice,
or referenced by the media as validated information.

Evolution of shear instability and multi-source precursor characteristics of soft–hard interbedded rock masses

Shili Xiao
Guizhou University
Shiwan Chen
swchen@gzu.edu.cn
Guizhou University
Wanxue Long
Guizhou University
Penghao Yu
Guizhou University
Dan Yang
Guizhou University

Article

Keywords: soft–hard interbedded rock mass, collapse, acoustic emission, digital image correlation, precursor information

Posted Date: November 16th, 2026

DOI: https://doi.org/10.21203/rs.3.rs-11547229/v1

License: This work is licensed under a Creative Commons Attribution 4.0 International License.
Read Full License

Additional Declarations: No competing interests reported.

Evolution of shear instability and multi-source precursor characteristics of soft–hard interbedded rock masses

Shili Xiao[1,2], Shiwan Chen[1,2,*], Wanxue Long[1], Penghao Yu[1,2], Dan Yang[1,2]

1. The College of Resources and Environmental Engineering, Guizhou University, Guizhou Guiyang 550025, China;
2. Key Laboratory of Karst Georesources and Environment, Ministry of Education, Guizhou University, Guizhou Guiyang 550025, China

Corresponding author: Shiwan Chen, swchen@gzu.edu.cn. Tel: +86-18875208337

Abstract: To address the difficulty of reliably identifying instability precursors during collapse development in soft–hard interbedded rock masses using a single monitoring parameter, two large-scale shear tests were conducted on soft–hard interbedded composite specimens. Digital image correlation (DIC), acoustic emission (AE), RA–AF analysis, and principal component analysis–hierarchical cluster analysis (PCA–HCA) characterized deformation and fracture evolution. Both specimens exhibited four stages: soft-rock compaction, coordinated deformation, crack propagation, and crack coalescence and instability. DIC revealed that scattered high-strain zones progressively localized near interfaces and flaw tips, ultimately forming a continuous band. RA–AF analysis indicated that tensile or mixed tensile–shear events dominated the first two stages, whereas shear-type events exceeded 50% during crack propagation. PCA–HCA classified AE signals into five types. Type 4 signals increased abruptly during crack development and coalescence and exhibited shear-fracture characteristics. Rapid expansion and incipient connection of high-strain zones, an increased shear-event proportion, and an abrupt rise in the Type 4 proportion constituted a multi-source precursor criterion for the transition from coordinated deformation to crack propagation. These findings provide an experimental basis for stage identification and monitoring-based early warning of collapse in soft–hard interbedded rock masses.

Keywords: soft–hard interbedded rock mass; collapse; acoustic emission; digital image correlation; precursor information

1 Introduction

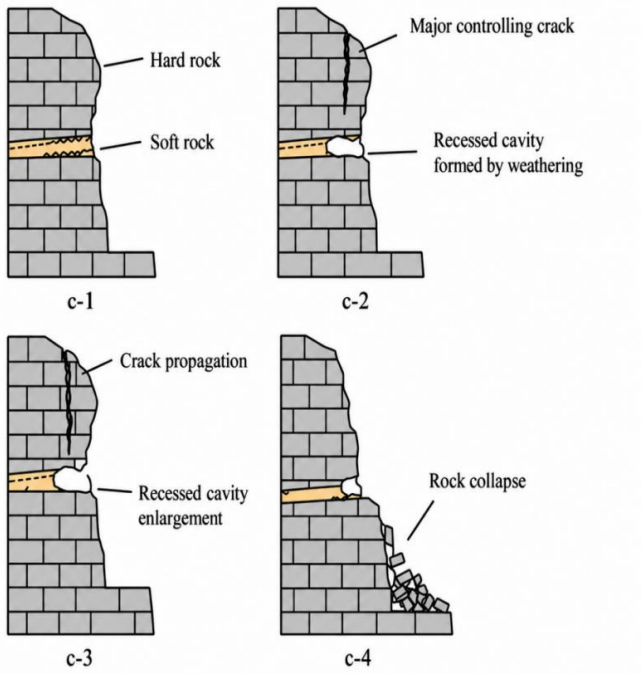
Karst is widely developed in southwestern China, where carbonate rocks are interbedded with weak argillaceous and silty strata, forming typical soft–hard interbedded structures. Long-term differential weathering causes the weak strata to progressively retreat and form recesses, altering the support conditions and stress distribution of the overlying rock mass. As shown in Fig. 1, the interaction between recess development and the propagation of controlling fractures can induce shear slip in local unstable rock masses and ultimately lead to collapse. Layer combinations, thickness ratios, and interlayer structures are important factors affecting the deformation and failure of these rock masses [1–7]. During the development of collapse, local crack activity does not necessarily produce obvious overall displacement, whereas crack propagation and rock-bridge failure can generate elastic-wave signals. Combining fracture-related acoustic signals with deformation information to identify the evolution of controlling fractures from propagation to coalescence is therefore an important approach to investigating shear-instability precursors in soft–hard interbedded rock masses.



(a) July 17 rock collapse in Pengshui, Chongqing



(b) Collapse at Xingfa Coal Mine, Zhijin



(c) Schematic of the development of shear-type collapse in soft–hard interbedded rock masses

Fig. 1 Formation of unstable rock masses and collapse in soft–hard interbedded strata

Progressive instability in soft–hard interbedded rock masses is closely associated with deformation incompatibility caused by lithological contrasts and the control of interlayer structures on crack paths. Studies of toppling deformation and stability in layered slopes have shown that layer combinations alter the locations of concentrated deformation and the progression from local failure to overall instability [1–6]. At the material scale, Liu et al. [7] used three-point bending tests to reveal the effects of layer combinations on the fracture behavior of soft–hard interbedded rock layers. Luo et al. [8] and Xie et al. [9] investigated deformation and failure characteristics at different layer thickness ratios, demonstrating that mutual restraint between soft and hard layers is important for understanding the response of composite specimens. Experiments on interface roughness, layer thickness ratios, and bedding conditions further showed that interlayer interfaces and structural parameters jointly affect stress transfer, crack propagation, and failure modes [10–14]. Cyclic loading tests on jointed soft–hard composite rocks revealed fatigue damage and the associated AE response [15], while shear tests on bonded rock–concrete interfaces demonstrated the effects of normal confinement on shear properties and AE characteristics from the perspective of interface loading [16]. These studies provide a basis for understanding damage evolution under interlayer contrasts and interface constraints. However, findings obtained under toppling, compression, or tension cannot directly describe shear instability under the combined action of recesses, controlling fractures, and interlayer weak planes. Experiments under the corresponding structural and loading conditions are still required to reveal the characteristics of crack development and coalescence.

Acoustic emission (AE) monitoring records elastic waves generated by internal rock fracture, providing experimental evidence linking crack activity to instability stages. Combined monitoring tests on flawed rock specimens and rock-bridge structures have shown that AE activity can be compared with surface cracking and deformation evolution [17–19]. Building on this approach, Pan et al. [20] and Li et al. [21] investigated tensile–shear failure responses associated with joint geometry and complex stress states, respectively, indicating that acoustic signal characteristics need to be interpreted in relation to specific structural and loading conditions. Bi et al. [22] investigated crack

classification and precursor indices using RA–AF parameters, while Wang et al. [23] used machine learning to identify tensile–shear fracture signals, extending analyses of event counts and energy changes to fracture-mode identification. Studies involving different lithologies, flaws, and loading conditions also reflect the relationship between AE responses and cracking mechanisms, as well as its dependence on experimental conditions [24–27]. Combined observations of mechanical behavior, acoustic activity, and surface deformation provide additional evidence for examining this relationship [28–30]. Precursor identification therefore requires attention to both the temporal evolution of acoustic signals and the corresponding fracture processes. An anomaly in a single parameter is insufficient to explain the evolution of instability in complex rock masses.

Multiparameter AE classification provides an additional means of identifying different fracture activities and their evolution through successive stages. Xie et al. [31] combined clustering with convolutional neural networks to extract AE precursor information from rock masses containing a single fracture. Yang et al. [32] investigated AE characteristics and early-warning information in fractured layered limestone, demonstrating that signal types and their temporal evolution can be used to analyze the failure process. Karimpouli et al. [33] characterized the temporal evolution of laboratory seismic-event features through unsupervised clustering, and Matochkina et al. [34] discussed AE-event clustering parameters in laboratory rock-fracture experiments, further demonstrating the feasibility of identifying characteristic groups from multiparameter signals. Principal component analysis (PCA) compresses correlated parameters while retaining the main information, whereas hierarchical cluster analysis (HCA) classifies signal types according to feature similarity. Combining the two methods facilitates analysis of changes in the types of large numbers of AE events. Deformation monitoring using fiber Bragg gratings also provides independent observational evidence of crack development [35]. Previous studies have expanded the methods available for classifying fracture signals. Nevertheless, statistical differences among signal clusters must be related to actual crack propagation and deformation processes before they can be assigned clear mechanical meanings and used for stage identification.

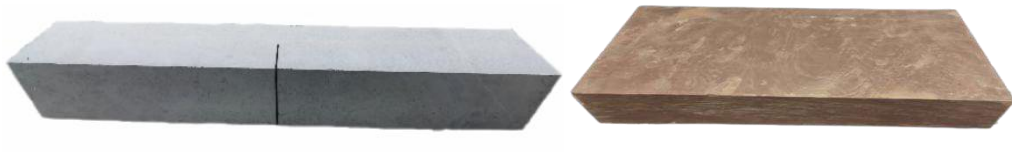
Field microseismic monitoring has progressed from detecting fracture activity to analyzing instability mechanisms and providing spatiotemporal early warnings, offering case-based evidence for the use of acoustic signals in rock-collapse and slope monitoring. Amitrano et al. [36] analyzed records preceding the collapse of a chalk cliff in Normandy, France, and found accelerating microseismic event rates and energy, together with increasing mean event size, as failure approached. These observations reflected the progression of damage towards macroscopic instability. Senfaute et al. [37] further identified event families with different spectral characteristics before collapse and associated the progressive loss of high-frequency components with crack initiation, propagation and coalescence, and activity along larger fractures. Their findings provided a basis for interpreting failure stages through changes in signal types. Occhiena et al. [38] combined similar-waveform grouping, source localization, and rock-mass structural analysis to identify areas in the Matterhorn monitoring data that could be controlled by a common fracture mechanism, linking acoustic signal analysis to potential instability locations. Feng et al. [39] used rockfall detection, classification, and localization results from a limestone quarry in Italy to establish a spatiotemporal early-warning framework based on cumulative seismic energy generated by rolling and impacts, and evaluated its performance through retrospective analysis. These cases demonstrate the monitoring value of fracture-source activity and rockfall-motion information, respectively. However, the two types of signals represent different physical processes, and their associated indices are affected by site structure and propagation conditions. For soft–hard interbedded rock masses, controlled experiments are still needed to establish relationships among acoustic signal types, crack propagation, and deformation localization, providing a basis for interpreting field criteria.

Based on these considerations, this study investigates soft–hard interbedded composite rock masses through simulated shear tests under normal confinement, using large specimens containing recesses and prefabricated controlling flaws. Load, shear displacement, and AE signals were recorded synchronously. Digital image correlation (DIC) was used to obtain surface displacement and strain fields, linking internal fracture activity to surface deformation evolution. RA–AF crack-mode analysis and PCA–HCA multiparameter signal classification were then combined to investigate changes in signal types and their mechanical implications during the development and coalescence of controlling fractures. Stage-specific precursors jointly represented by acoustic signals and deformation information were identified, providing an experimental basis for monitoring criteria for shear instability in soft–hard interbedded rock masses.

2 Materials and experimental methods

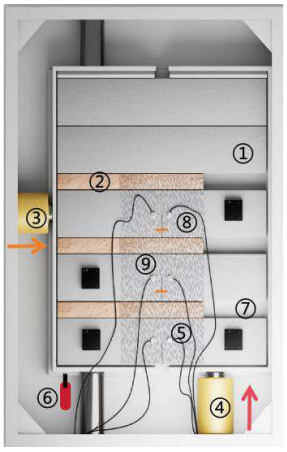
2.1 Specimen preparation and structural design

Limestone and silty mudstone from the Lower Triassic Yelang Formation (T_1y) in Guizhou were selected as the experimental materials to represent the hard and soft layers, respectively, in the soft–hard interbedded structure. The basic mechanical properties of the two rock materials are listed in Table 1. The limestone used in the tests had markedly higher elastic modulus, uniaxial compressive strength, and tensile strength than the silty mudstone. The limestone specimens measured 1000 mm × 150 mm × 150 mm, with a 3-mm-wide flaw prefabricated at the center to simulate the main fracture controlling collapse. The silty mudstone specimens measured 400 mm × 150 mm × 50 mm. The limestone and silty mudstone were combined to form a soft–hard interbedded structure, and black speckles were applied over a white background in the observation area for DIC image acquisition and strain-field monitoring. The specimens were assembled by alternately stacking limestone and silty mudstone to simulate a soft–hard interbedded rock mass, with a cavity representing the recess in a collapsing rock mass.



(a) Hard-rock specimen (b) Soft-rock specimen





(c) Experimental apparatus (d) Schematic of the soft–hard interbedded composite specimen

Fig. 2 Specimens and experimental apparatus

Table 1 Physical and mechanical properties of limestone and silty mudstone

Material	Elastic modulus (GPa)	Uniaxial compressive strength (MPa)	Tensile strength (MPa)
Limestone	18~23	110~115	6.1~6.3
Silty mudstone	1.0~1.1	12~14	0.5~0.7

2.2 Experimental apparatus and procedures

As shown in Fig. 2(c) and (d), the experiments were conducted using a large-scale shear loading system consisting primarily of normal and tangential loading units, a displacement acquisition system, and a monitoring system. The system applies normal and tangential loads to large specimens. The controlling fracture surfaces involved in collapse hazards in soft–hard interbedded rock masses are subject to normal confinement. A constant normal load was therefore maintained throughout the shear tests to simulate the shear response under confined conditions. The normal load was 50 kN. Tangential loading was applied incrementally, with a 3 kN load increment followed by a 5 min hold at each level. Tangential load and shear displacement were recorded synchronously during loading. DIC was used to record the surface strain field, while AE monitoring captured the evolution of acoustic signals released during crack propagation.

The AE monitoring system continuously recorded crack development during shear loading. A PCI-2E5.40 AE acquisition system with a center frequency of 150 kHz was used. AE sensors were placed near the prefabricated flaw and firmly coupled to the specimen surface using a coupling agent to ensure signal acquisition quality. The DIC monitoring system measured the surface displacement and strain fields during shear loading. Before testing, black speckles were applied over a white background on the observation surface. During loading, a camera continuously acquired images of the specimen surface to identify surface deformation localization and the propagation paths of high-strain zones. Displacement sensors simultaneously recorded shear displacement for comparison with the load–displacement curves, AE activity, and DIC strain-field results.

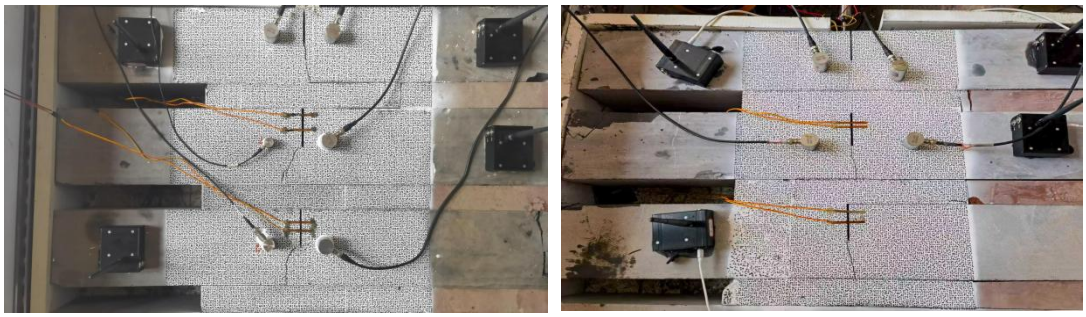
3 Results and discussion

3.1 Macroscopic failure characteristics and mechanical response

Figure 3 shows the macroscopic crack patterns of the two soft–hard interbedded composite specimens after failure. Figure 4 presents the displacement monitoring results during shear loading. At the beginning of loading, the shear load increased slowly with displacement, and the curves were relatively flat. This stage mainly corresponded to the closure of pre-existing microcracks, adjustment of interlayer contacts, and recompaction of soft–hard rock interfaces, with no obvious propagation of newly formed cracks at the macroscopic scale. As the shear load continued to increase, the load–displacement curves gradually changed from approximately linear growth to nonlinear evolution. Internal damage began to accumulate steadily, and cracks progressively initiated and propagated at prefabricated flaw tips, interlayer interfaces, and local stress concentrations. Near the peak load, the curve slopes changed markedly and shear displacement accelerated, indicating a transition from local crack propagation to accelerated linkage and coalescence.

The failure patterns indicate that macroscopic failure of the soft–hard interbedded composite specimens did not occur through overall sliding along a single weak layer. Instead, it was jointly controlled by the prefabricated flaws, interlayer interfaces, and lithological contrasts. Cracks initially developed preferentially within the hard-rock layers, then propagated towards neighboring soft-rock layers and interlayer interfaces. At a later stage, multiple local cracks connected to form a

through-going failure surface. As indicated in Table 1, the higher elastic modulus, compressive strength, and tensile strength of limestone made it more likely to develop controlling crack paths and dominate through-going failure during shearing. The silty mudstone, with lower strength and stiffness, mainly accommodated local deformation and buffered crack propagation.



(a)HC1 (b)HC2

Fig. 3 Shear failure patterns of the soft–hard interbedded specimens

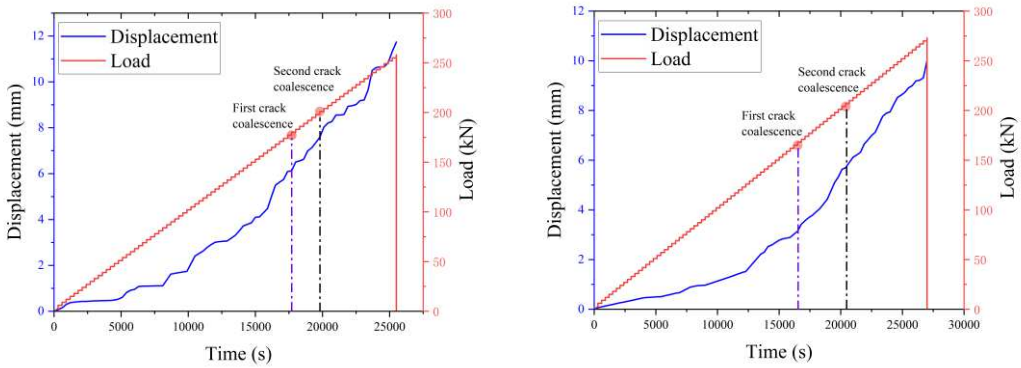


Fig. 4 Shear time–load–displacement curves of the soft–hard interbedded specimens

Overall, under the experimental conditions used in this study, the formation and coalescence of the main cracks in both HC1 and HC2 were primarily controlled by the hard-rock layers and prefabricated flaws. The soft-rock layers and interlayer interfaces played important roles in regulating crack deflection, cross-layer linkage, and local slip. This macroscopic failure pattern provides a mechanical basis for the subsequent AE-based identification of crack-mode transitions and instability precursors.

3.2 Strain fields and acoustic emission throughout shear fracture

3.2.1 Stage-dependent evolution

Figure 5 shows the evolution of the strain field and AE activity in specimen HC1 during shear loading. Overall, the soft–hard interbedded composite specimen did not undergo instantaneous instability along a single continuous sliding surface. Instead, it evolved progressively through local strain anomalies, stable propagation, rapid linkage, and coalescence-induced instability. Based on stage-dependent changes in the surface strain field and AE activity, the shear failure of HC1 was divided into four stages: soft-rock compaction (Stage I), coordinated deformation (Stage II), crack propagation (Stage III), and crack coalescence and instability (Stage IV).

During the soft-rock compaction stage (Stage I), the overall stress level and AE activity were low. High-strain responses were mainly concentrated at interlayer interfaces and within the soft rock, while no distinct deformation band had formed around the prefabricated flaw. In the coordinated deformation stage (Stage II), pronounced strain localization appeared around the prefabricated flaw in the hard rock and within the soft rock. High-strain zones became concentrated into bands,

accompanied by increased AE activity. In the crack propagation stage (Stage III), strain concentration near the prefabricated flaw became more pronounced, and local high-strain zones began to connect. These zones developed along the prefabricated flaw, interlayer interfaces, and locally weak regions. AE activity increased markedly, with more high-amplitude events. In the crack coalescence and instability stage (Stage IV), surface high-strain zones connected to form a continuous strain-localization band crossing multiple layers. Macroscopic cracks extended along the prefabricated flaw and coalesced through the intervening rock layers, forming a composite failure path. The strain band exhibited changes in direction, offsets, and local curvature at hard–soft rock boundaries, indicating that interlayer mechanical contrasts regulated crack propagation paths.

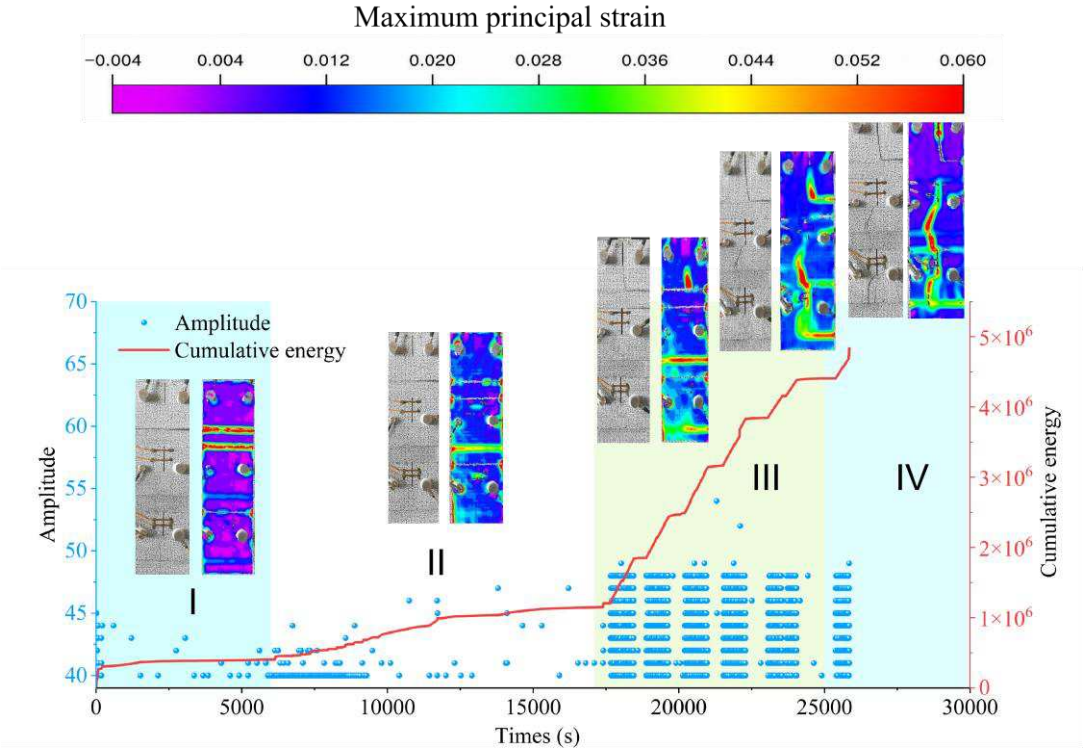


Fig. 5 Evolution of acoustic emission and strain fields during specimen shearing

3.2.2 Evolution of crack modes based on RA–AF analysis

RA–AF parameters were used to identify the crack modes of AE events and analyze stage-dependent changes in crack activity, as shown in Fig. 6. RA is the ratio of rise time to amplitude, and AF is the ratio of ring-down counts to duration. Signals with low RA and high AF are more indicative of tensile cracking, whereas those with high RA and low AF are more indicative of shear cracking. RA–AF analysis is an indirect identification method based on waveform parameters, and its classification is affected by material heterogeneity, sensor arrangement, propagation paths, wave attenuation, and threshold settings. Accordingly, it was used here only to analyze relative changes in crack modes between stages, rather than to determine the fracture mechanism of an individual AE event definitively.

$$RA=\frac{RT}{A} \tag{1}$$

$$AF=\frac{N_c}{D} \tag{2}$$

An empirical boundary with a slope of 1 in the RA–AF plot was used to classify crack modes. Events above the boundary were classified as tensile-type events, and those below it as shear-type

events. Changes in the proportions of the two event types were quantified for Stages I–IV. This classification was intended to identify shifts in crack activity across loading stages.

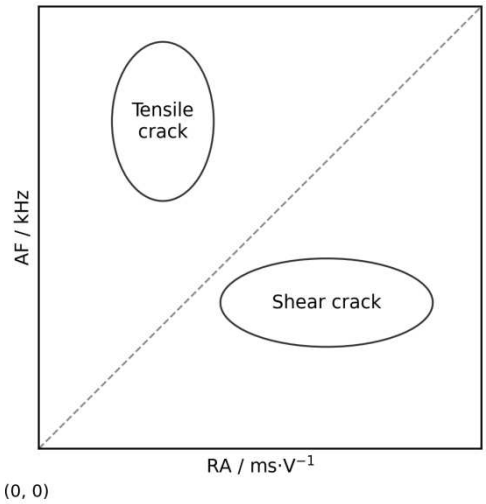


Fig. 6 Crack-mode identification based on RA–AF parameters

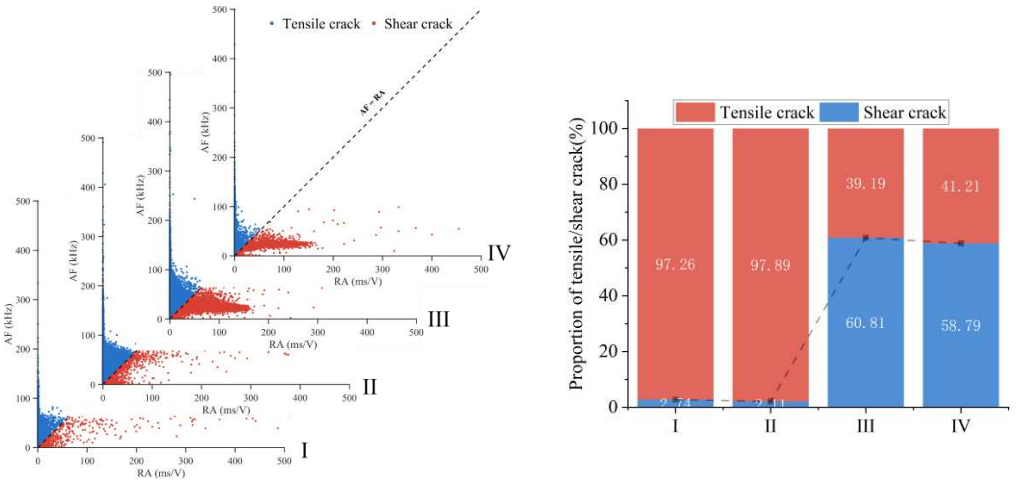
As shown in Fig. 7, AE events in HC1 and HC2 during Stage I (soft-rock compaction) were mainly located in the low-RA, high-AF region, with tensile-type events overwhelmingly dominant. Tensile-type events accounted for approximately 97.26% and 97.41% of the events in HC1 and HC2, respectively, whereas the proportions of shear-type events were low. Damage during initial loading was mainly associated with local opening of pre-existing microdefects and consisted primarily of small-scale tensile fractures.

During Stage II (coordinated deformation), tensile-type events remained dominant in both specimens, accounting for approximately 97.89% and 97.01% of the events in HC1 and HC2, respectively. Compared with Stage I, the number of AE events increased as microcracks continued to initiate and propagate steadily. Nevertheless, the RA–AF distributions remained concentrated in the tensile region, indicating that crack activity was still characterized by tensile initiation and local damage accumulation.

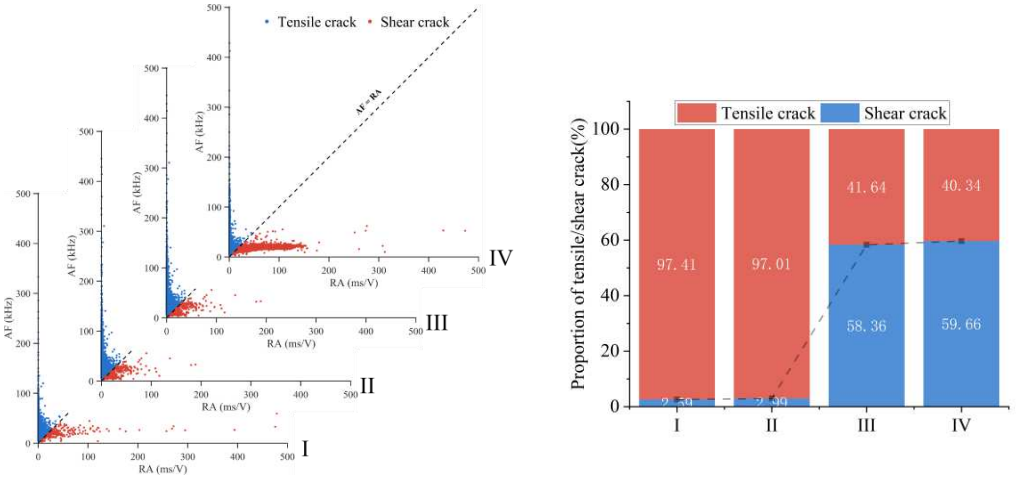
During Stage III (crack propagation), the RA–AF distributions shifted markedly towards the high-RA, low-AF region, and the proportions of shear-type events increased substantially. These proportions reached approximately 60.81% and 58.36% in HC1 and HC2, respectively, exceeding the proportions of tensile-type events. Fracture activity gradually changed from predominantly tensile initiation to mixed tensile–shear cracking, with shear propagation becoming dominant.

During Stage IV (crack coalescence and instability), shear-type events remained dominant, accounting for approximately 58.79% and 59.66% of the events in HC1 and HC2, respectively. AE events were mainly distributed in the high-RA, low-AF region, indicating that internal crack activity had shifted from scattered initiation and local propagation to concentrated failure dominated by shear slip, crack linkage, and local coalescence. The proportions of shear-type events remained high relative to Stage III, showing that shear fracture continued to dominate the final instability stage.

The RA–AF results indicate that crack modes in the soft–hard interbedded composite specimens evolved through tensile initiation, stable propagation, shear enhancement, and shear coalescence. Early tensile-type events were mainly associated with local opening of microdefects, crack initiation at prefabricated flaw tips, and adjustment of interlayer contacts. The increase in shear-fracture events during the crack propagation stage can provide precursor information for coalescence-induced instability.



(a) Proportions of tensile/shear cracks in HC1



(b) Proportions of tensile/shear cracks in HC2

Fig. 7 RA–AF distributions and crack-mode proportions at different stages in the soft–hard interbedded specimens

3.3 PCA–HCA method for identifying AE signal types

Principal component analysis (PCA) compresses multiparameter information by extracting mutually orthogonal composite variables, thereby reducing redundancy arising from correlations among parameters. Hierarchical cluster analysis (HCA) progressively merges samples according to their similarity in feature space to identify signal groups with similar response characteristics. Here, the two methods were combined by first reducing the dimensionality of the AE parameters and then clustering the principal component scores to analyze the composition of signal types at different failure stages. The preceding analyses of temporal AE responses and RA–AF crack modes revealed distinct stage-dependent fracture characteristics during shear loading of the soft–hard interbedded composite specimens. However, a single AE parameter cannot provide robust and reliable precursor information for through-going rock fracture. PCA–HCA was therefore used to classify multiparameter AE signals [32] and investigate their characteristics at each stage.

Rise time, energy, duration, peak frequency, amplitude, and mean frequency were selected as classification inputs to characterize the timescale, energy release, frequency structure, and intensity of AE events. Except for amplitude, the parameters differed considerably in magnitude and exhibited skewed distributions. They were therefore logarithmically transformed before standardization, as follows:

$$X_i' = log_{10}(X_i + 1) \tag{3}$$

$$Z_i = \frac{X_i' - \mu_i}{\sigma_i} \quad (4)$$

PCA was then used for dimensionality reduction, and the principal component scores accounting for at least 80% of the cumulative explained variance were used as inputs to HCA. The cumulative explained variance of PC1 and PC2 was 85.23% for HC1 and 80.95% for HC2. Figure 8 presents the PCA results for HC1, showing that the first two principal components retained the main information distinguishing the multiparameter AE signals.

Table 2 shows that the multiparameter AE signals exhibit continuous evolution. Based on the Davies–Bouldin index, Calinski–Harabasz index, and mean silhouette coefficient, K = 5 was considered appropriate.

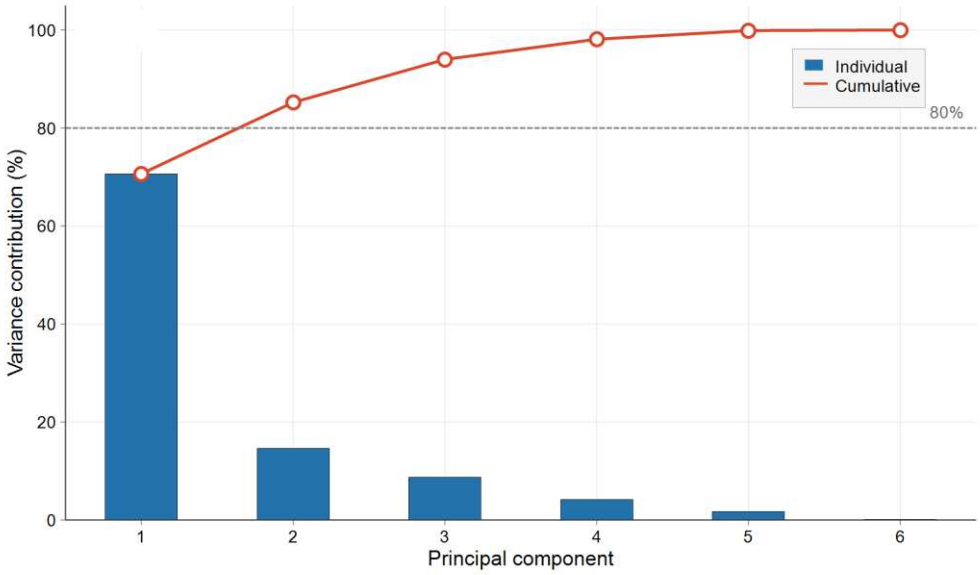


Fig. 8 Explained variance of the principal components

Table 2 PCA–HCA clustering validity for different numbers of clusters

Specimen	K	Mean silhouette coefficient	CH index	DB index
HC1	4	0.5300	4489.56	0.6752
HC1	5	0.5513	4787.10	0.7040
HC1	6	0.5573	4756.31	0.6881
HC1	7	0.5615	5032.42	0.6578
HC2	4	0.4839	4270.77	0.6613
HC2	5	0.4952	4592.90	0.7007
HC2	6	0.4879	4770.54	0.7459
HC2	7	0.5121	5246.96	0.7408

Note: A larger mean silhouette coefficient indicates greater separation between samples. A larger CH index indicates better intercluster separation and intracluster compactness, whereas a smaller DB index indicates better clustering performance.

Figure 9 presents the hierarchical clustering dendrogram. The vertical axis represents the Euclidean distance between AE signal samples, with larger distances indicating greater differences in their features. Based on the dendrogram branch structure and the trial results for different K values, the AE signals were divided into five clusters at the cut height marked by the red dashed line.

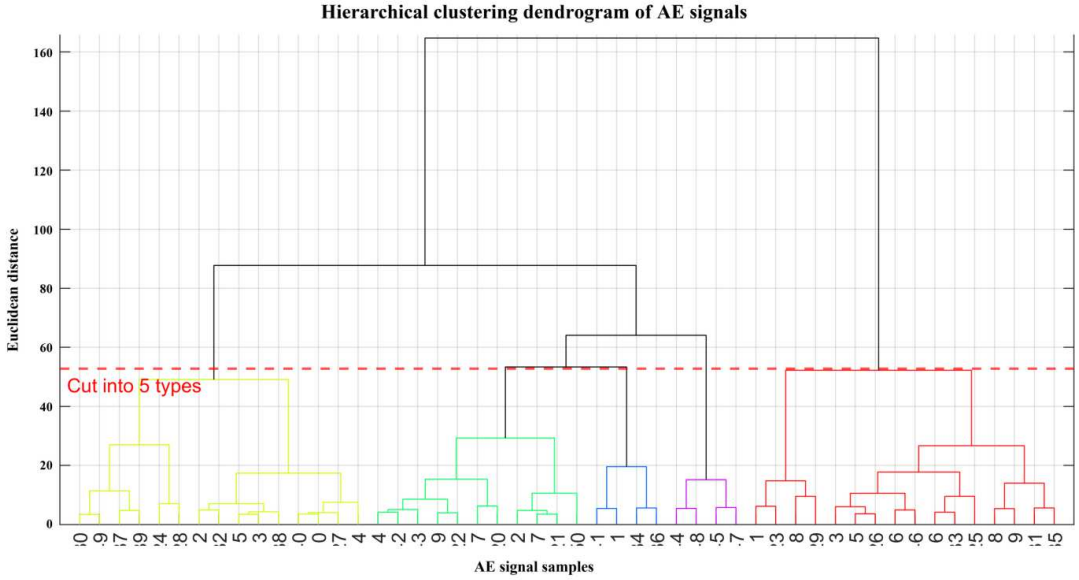


Fig. 9 Hierarchical clustering dendrogram and cut height for K = 5

3.3.1 PCA–HCA-based identification of AE signal types and analysis of instability precursors

Table 3 summarizes the number of AE events (N), amplitude, RA, AF, and shear-type event proportion (Shear-type/%) for each signal type. Here, N denotes the number of AE events of a given type, and Amplitude denotes their within-type mean amplitude. RA and AF denote the within-type means of the rise-time-to-amplitude ratio and the ring-down-count-to-duration ratio, respectively. The shear-type event proportion is the percentage of events classified as shear-type by the RA–AF criterion among all events of that signal type.

Table 3 Multiparameter statistical characteristics of different AE signal types

Specimen	Type	N	Amplitude (dB)	RA	AF	Shear-type/%
HC1	Type1	119534	41.46	0.08	835.81	0.00
HC1	Type2	106270	42.88	10.13	17.98	37.25
HC1	Type3	64654	46.12	59.71	18.22	83.58
HC1	Type4	203343	45.47	65.12	17.41	91.96
HC1	Type5	520	73.92	39.53	36.03	32.88
HC2	Type1	119328	42.33	0.02	905.37	0.00
HC2	Type2	85188	42.75	0.54	59.46	0.00
HC2	Type3	69428	45.02	4.49	28.13	11.82
HC2	Type4	182200	46.88	59.78	21.59	87.18
HC2	Type5	135258	48.29	59.40	22.69	84.03

Figure 10 shows the distributions of Type 1–Type 5 in the PC1–PC2 plane. Although adjacent types overlap to some extent at their boundaries, the signal types generally exhibit identifiable clustering and spatial separation. This indicates that HCA using principal component scores

accounting for at least 80% of the cumulative explained variance can characterize the main structural differences among multiparameter AE signals.

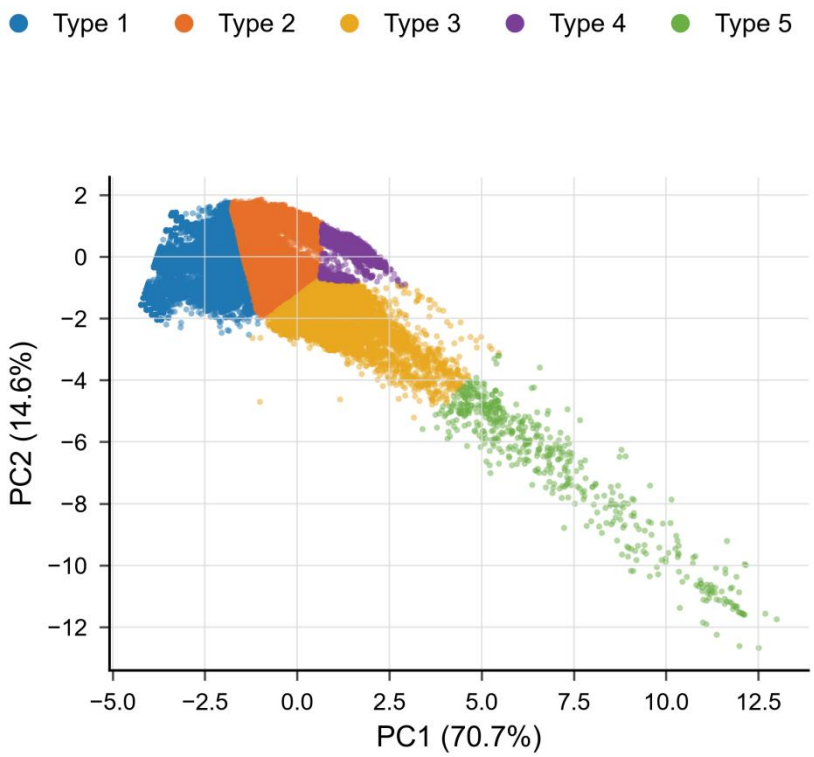


Fig. 10 Scatter plot of PCA–HCA classification results

Figure 11 shows the proportions of Type 1–Type 5 signals at different failure stages. During loading-induced deformation and failure of HC1, Type 4 accounted for only 0.20% and 0.18% of the signals in Stages I and II, respectively. Its proportion increased rapidly to 43.54% in Stage III and remained high at 41.82% in Stage IV. Acoustic signals during loading-induced deformation and failure of HC2 exhibited similar characteristics. The proportion of Type 4 was 3.20% in Stage I and 5.65% in Stage II, increasing to 36.74% in Stage III and further to 43.07% in Stage IV. The abrupt increase in Type 4 signals during crack propagation and coalescence-induced failure indicates that they are an important indicator of crack propagation and coalescence in rock masses. By contrast, although Type 5 accounted for 26.37% and 21.65% of the signals in HC2 during Stages III and IV, respectively, it was already abundant in Stages I and II, accounting for 15.34% and 10.74%, respectively, and therefore provided poorer discrimination. The transition of Type 4 from a low to a high proportion in both specimens provides precursor information indicating crack propagation and instability.

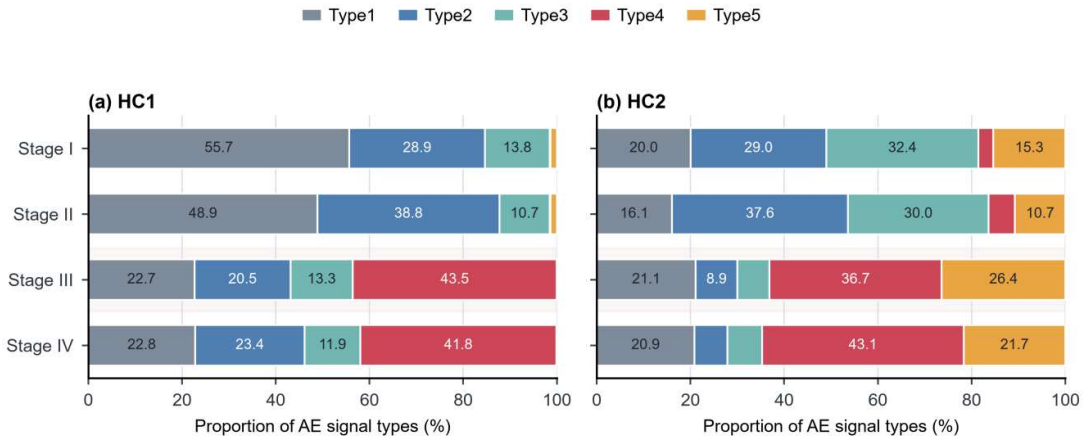
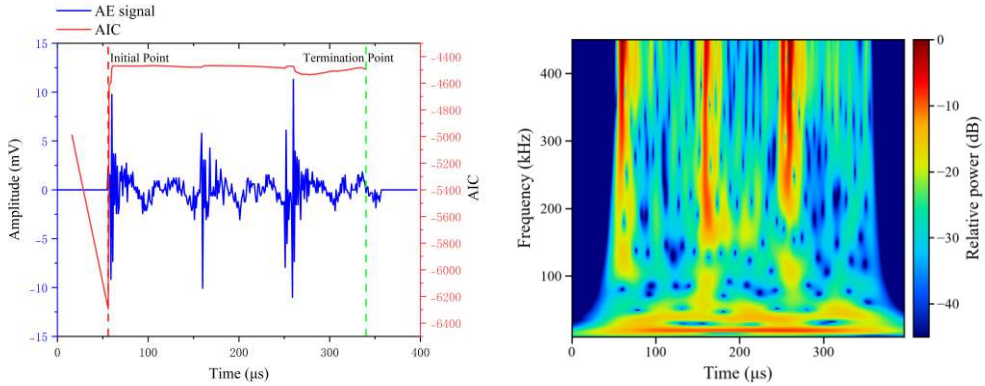


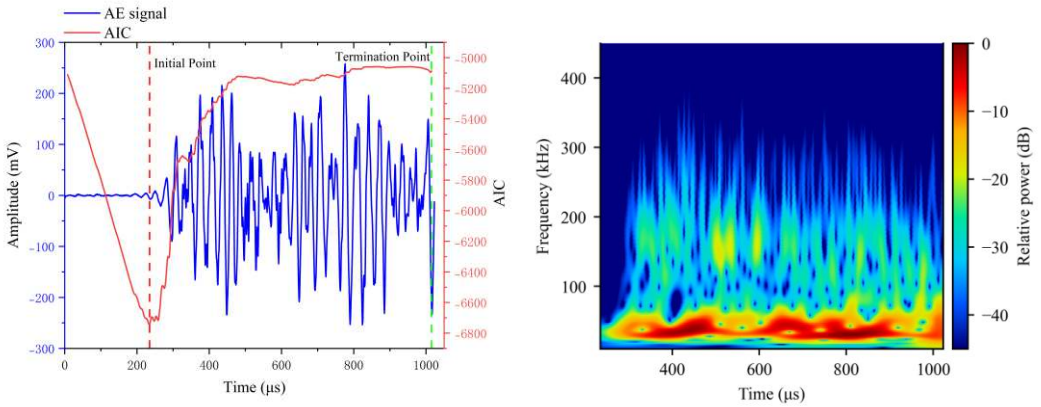
Fig. 11 Composition of AE signal types at different failure stages in specimens HC1 and HC2

Type 2 occurred in relatively large proportions at all stages of loading-induced specimen failure, limiting its value as a precursor of the fracture-development stage within the rock. In contrast, the evolution of the cumulative Type 4 curve was closely associated with the crack propagation stage. Representative waveforms of these two signal types were therefore selected for further analysis. The Akaike information criterion (AIC) was first used to identify the first-arrival times of the representative waveforms, as shown in Figs. 12(a) and 13(a). Comparison showed that Type 2 signals had short durations and low energy, exhibiting typical tensile-cracking characteristics, whereas Type 4 signals had long durations and high energy, corresponding to typical shear-fracture characteristics. To reveal their spectral characteristics, the AE waveforms of the two types were subjected to time–frequency analysis using a wavelet transform [40]. As shown in Figs. 12(b) and 13(b), the energy of Type 2 was mainly dispersed over 0–400 kHz. By contrast, the high-energy AE waves of Type 4 were broadly concentrated within 0–100 kHz, exhibiting continuous low-frequency, high-energy characteristics. Such low-frequency, high-energy signals commonly originate from shear fracturing and are closely associated with crack propagation and coalescence.



(a) Waveform with AIC arrival picking (b) Time–frequency spectrum

Fig. 12 Waveform and spectrum of Type 2 signals



(a) Waveform with AIC arrival picking (b) Time–frequency spectrum

Fig. 13 Waveform and spectrum of Type 4 signals

To further investigate the evolution of Type 4 signals throughout loading-induced fracture, the temporal evolution of their sliding-window proportion over the entire failure process was analyzed, as shown in Fig. 14. The proportion of Type 4 remained generally low during Stages I–II, increased rapidly after the onset of Stage III, and remained high throughout Stages III–IV. In HC2, for example, the proportion rapidly exceeded 30% after the onset of Stage III and repeatedly reached 40%–45% during Stage IV. This indicates that Type 4 was not an isolated local anomaly but a dominant AE response that remained active during crack propagation and crack coalescence and instability.

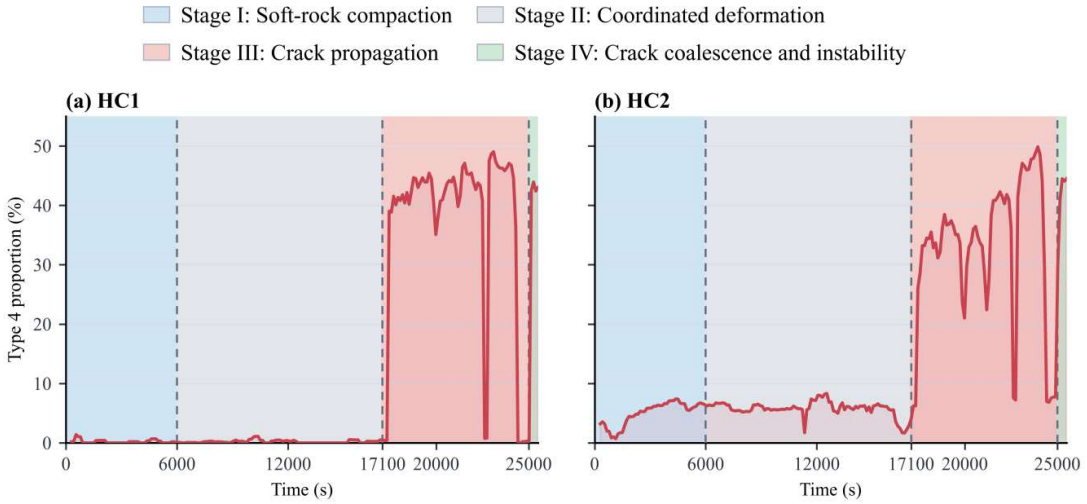


Fig. 14 Temporal evolution of the sliding-window proportion of Type 4 signals

Taken together, the PCA–HCA results reveal distinct stage-dependent changes in AE signal composition during shear instability. Stage I (soft-rock compaction) and Stage II (coordinated deformation) were dominated by tensile microfracturing, with local microcrack initiation and stable accumulation. In Stage III (crack propagation), the proportion of Type 4 signals increased abruptly. Their long durations, high energy, and low frequencies indicated an increase in relatively large-scale shear fractures within the rock mass. In Stage IV (crack coalescence and instability), Type 4 signals remained abundant, accompanied by some high-energy Type 5 signals, reflecting the joint contributions of shear coalescence and intense local fracturing to final instability.

The sustained increase in the proportion of Type 4 signals can therefore serve as an important precursor indicator of the transition from coordinated deformation to crack propagation in soft–hard interbedded composite specimens. PCA–HCA is not intended to predict the exact time of final failure but can be used to identify stages of crack development. Considering the stage-dependent

enhancement of Type 4 AE signals during crack propagation and coalescence together with the rapid local concentration of DIC strain and the increased proportion of shear-type events indicated by RA–AF analysis, Type 4 enhancement can serve as an important parameter for identifying the crack propagation stage preceding shear instability in soft–hard interbedded rock masses.

4 Discussion

Shear failure of the soft–hard interbedded composite specimens evolved continuously from contact adjustment through local crack initiation and linkage to coalescence-induced instability. During the soft-rock compaction stage (Stage I), adjustment within the weak layers and at interlayer contacts dominated. DIC high-strain zones were scattered, RA–AF classification was dominated by tensile-type events, and the proportion of Type 4 was low. During the coordinated deformation stage (Stage II), the soft and hard layers carried the load jointly, and local deformation gradually accumulated at prefabricated flaw tips and near interlayer interfaces. DIC strain began to localize, but neither shear-type events nor Type 4 signals showed sustained enhancement. These two stages corresponded to the initiation and accumulation of local damage, before the formation of a continuous shear-failure pathway.

During the crack propagation stage (Stage III), local cracks propagated towards interlayer interfaces and neighboring damaged regions, and high-strain zones expanded rapidly and began to connect. Meanwhile, the proportions of shear-type events exceeded 50% in both HC1 and HC2, and the proportion of Type 4 increased markedly from its earlier low level. These changes indicate concurrent enhancement of shear-related fracture activity and linkage of damaged zones. During the crack coalescence and instability stage (Stage IV), a continuous high-strain band formed and macroscopic shear failure occurred. Shear-type events remained dominant, and the proportion of Type 4 remained high. The different signals reflected surface deformation localization, crack-mode transitions, and changes in multiparameter AE composition, respectively. Their concurrent transitions constitute multi-source evidence for the development from local damage to through-going failure.

Based on these evolutionary patterns, Fig. 15 presents a multi-source precursor criterion comprising rapid expansion and incipient connection of surface high-strain zones, an increased proportion of RA–AF shear-type events, and a sustained increase in the sliding-window proportion of Type 4 signals. This criterion identifies the transition from coordinated deformation to crack propagation in soft–hard interbedded rock masses. Compared with a single displacement, AE energy, or crack-mode indicator, the combined criterion characterizes damage evolution before shear instability through surface deformation, crack modes, and AE signal composition, providing robust information for stage assessment and monitoring-based early warning.

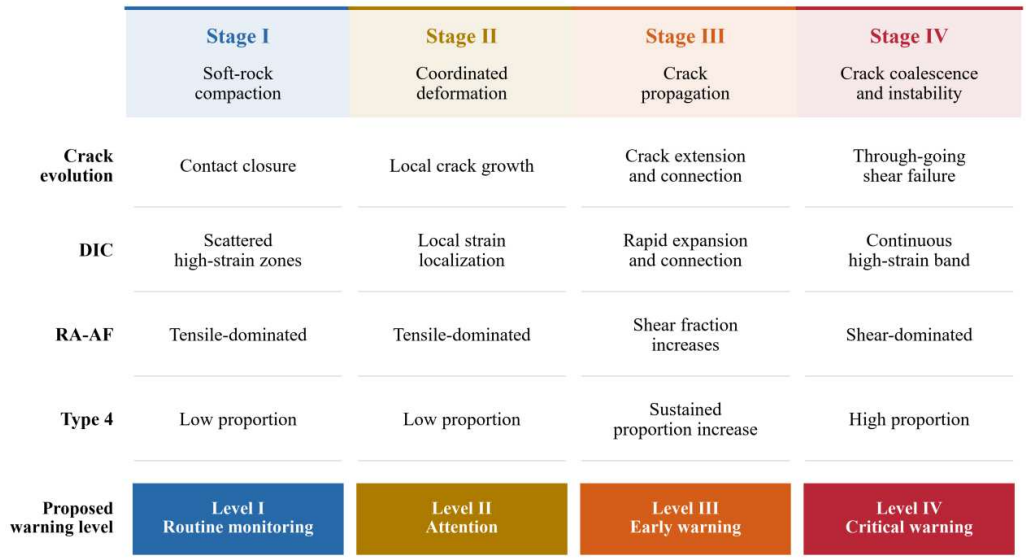


Fig. 15 Four-stage multi-source responses of soft–hard interbedded rock masses

5 Conclusions

To investigate the development of collapse in soft–hard interbedded rock masses, large-scale shear tests were conducted, and DIC, AE, RA–AF, and PCA–HCA analyses were used to characterize deformation and acoustic signals during specimen failure. The main conclusions are as follows:

(1) Based on the load–displacement response, crack development, and changes in AE activity, the shear failure of HC1 and HC2 can be divided into four stages: soft-rock compaction (Stage I), coordinated deformation (Stage II), crack propagation (Stage III), and crack coalescence and instability (Stage IV). Lithological contrasts and interlayer interfaces jointly affect local deformation accumulation, crack propagation, and the final coalescence paths.

(2) DIC observations show that initially scattered high-strain zones progressively concentrate near prefabricated flaw tips and soft–hard interfaces, then expand rapidly, connect, and form a continuous high-strain band. This process reveals the progression of surface deformation from local damage accumulation to through-going shear failure.

(3) AE parameters reflect the transition of crack activity modes across loading stages. RA–AF statistics show that tensile-type events dominate Stages I–II. In Stage III, the proportions of shear-type events in HC1 and HC2 increase to 60.81% and 58.36%, respectively, and remain at 58.79% and 59.66% in Stage IV, corresponding to the continued development of shear slip, crack linkage, and through-going failure.

(4) PCA–HCA classifies AE signals into five types, Type 1–Type 5. Type 4 exhibits relatively high RA, low AF, and a high proportion of shear-type events. Its proportion increases from 0.18% (HC1) and 5.65% (HC2) in Stage II to 43.54% and 36.74%, respectively, in Stage III, and remains high in Stage IV. Compared with Type 2, which can occur throughout the entire process, and Type 5, which already accounts for a considerable proportion in the early stages of HC2, the transition of Type 4 from a low to a persistently high proportion corresponds more clearly to the crack propagation stage and can serve as a candidate indicator for stage identification.

(5) Integrating the DIC, RA–AF, and PCA–HCA results, a four-stage multi-source response and proposed graded early-warning model is developed. The concurrent rapid expansion and incipient connection of high-strain zones, increase in the proportion of shear-type events, and

sustained increase in the proportion of Type 4 signals can jointly identify the transition from coordinated deformation to crack propagation. A continuous high-strain band and macroscopic through-going failure characterize the instability stage. This model establishes a correspondence between experimental damage stages and early-warning responses, providing a basis for subsequent field threshold calibration.

Author contributions

Shili Xiao wrote the main manuscript text and prepared Figures 1–15. Shiwan Chen designed the research methodology, supervised the project, and revised the manuscript. Wanxue Long provided research materials. Penghao Yu participated in data analysis. Dan Yang was responsible for data organization and compilation. All authors reviewed and approved the final manuscript.

Funding

This work was supported by the National Natural Science Foundation of China (Grant No. 4216020116) and the Guizhou Provincial Major Science and Technology Project (Grant No. Qian Ke He Major Project [2024] 008).

Data availability

Some or all data, models, or code that support the findings of this study are available from the corresponding author upon reasonable request.

Competing interests

The authors declare no competing interests.

References

1. Huang, D., Ma, H. & Huang, R. Deep-seated toppling deformations of rock slopes in western China. *Landslides* **19**, 809–827 (2022).

2. Ning, Y. *et al.* A stability evaluation method for deep-seated toppling in the upper Lancang river, Southwestern China. *J. Rock Mech. Geotech. Eng.* **16**, 2388–2410 (2024).

3. Liu, Y., Huang, D., Peng, J. & Guo, Y. Analysis of the effect of rock layer structure on the toppling failure evolution of soft-hard interbedded anti-dip slopes. *Eng. Fail. Anal.* **145**, 107005 (2023).

4. Guo, J., Wu, Z. & Liu, K. Stability analysis of soft–hard-interbedded anti-inclined rock slope. *Sci. Rep.* **13**, 1643 (2023).

5. Guo, H. *et al.* Mechanical analysis of toppling failure using FDEM: A case study for soft-hard

505 interbedded anti-dip rock slope. *Comput. Geotech.* **165**, 105883 (2024).
506 6. Zhang, B. *et al.* Exploring the Deformation and Failure Characteristics of Interbedded
507 Anti-inclined Rock Slopes: Insights from Physical Modelling Tests. *Rock Mech. Rock Eng.* **57**,
508 1603–1628 (2024).
509 7. Liu, Y., Huang, D., Peng, J. & Yang, Y. Influences of layer combination on fracture behaviour
510 of soft–hard interbedded rock layers using three-point-bending test. *Theor. Appl. Fract. Mech.* **122**,
511 103671 (2022).
512 8. Luo, P., Li, D., Ma, J., Zhou, A. & Zhang, C. Experimental investigation on mechanical
513 properties and deformation mechanism of soft-hard interbedded rock-like material based on digital
514 image correlation. *J. Mater. Res. Technol.* **24**, 1922–1938 (2023).
515 9. Xie, Q. *et al.* Influence of Layer Thickness Ratio on the Mechanical and Failure Properties of
516 Soft-Hard Interbedded Rock-like Material. *KSCE J. Civ. Eng.* **27**, 4962–4977 (2023).
517 10. Li, J., Shi, X. & Su, C. Investigation of the macro-micro mechanical properties of soft–hard
518 interbedded rock-like materials considering varied interface roughness and layer thickness
519 proportions. *Unconv. Resour.* **9**, 100282 (2026).
520 11. Li, J.-H. *et al.* Experimental study on deformation and failure characteristics of soft and hard
521 composite rock masses with different layer thickness ratios. *Environ. Earth Sci.* **85**, 97 (2026).
522 12. Luo, P. *et al.* Influence of bedding plane on the tensile properties and crack propagation of soft
523 and hard laminated rock-like under Brazilian test. *Theor. Appl. Fract. Mech.* **127**, 104087 (2023).
524 13. Li, J.-H., Li, Y.-L., Wang, P., Liu, W.-X. & Yang, Y. Effect of thickness ratio on uniaxial
525 mechanical behavior of soft-hard composite rock masses: experimental analysis and modeling. *Sci.*
526 *Rep.* **15**, 44355 (2025).
527 14. Yang, C., Li, S., Feng, X., Wu, L. & Lin, H. Mechanical and Failure Behavior of Soft-Hard
528 Composite Rock with Three Parallel Joints Under Uniaxial Loading: Insights Based on AE and DIC
529 Techniques. *Materials* **18**, 1088 (2025).
530 15. Wang, Z., Li, S., Lin, H. & Chen, Y. Fatigue response and AE characteristics of soft and hard
531 composite rock containing coplanar double joints. *Int. J. Fatigue* **198**, 108994 (2025).
532 16. Chen, Y., Yang, J., Wang, J., Heng, S. & Hou, Z. Effects of normal stress on shear properties
533 and acoustic emission characteristics of bonded rock-concrete interfaces. *Sci. Rep.* **15**, 29081
534 (2025).

17. Zhao, Y., Chen, C., Wu, S., Guo, P. & Li, B. Effects of 2D&3D nonparallel flaws on failure characteristics of brittle rock-like samples under uniaxial compression: Insights from acoustic emission and DIC monitoring. *Theor. Appl. Fract. Mech.* **120**, 103391 (2022).

18. Fan, J. & Zhu, X. Systematic detection and evaluation of cracking behavior of flawed brittle sandstones with AE and 3D-DIC techniques. *PLOS ONE* **19**, e0309381 (2024).

19. Wang, J. *et al.* Damage-fracture evolution mechanism of rock bridge structures in flawed sandstone under cyclic disturbance: Insights from DIC-AE. *Theor. Appl. Fract. Mech.* **140**, 105180 (2025).

20. Pan, H. *et al.* Acoustic emission characteristics in tensile-shear failure of non-persistent jointed rocks with different undulation angles. *J. Cent. South Univ.* **31**, 1687–1699 (2024).

21. Li, S., Yang, D., Huang, Z., Gu, Q. & Zhao, K. Acoustic emission characteristics and failure mode analysis of rock failure under complex stress state. *Theor. Appl. Fract. Mech.* **122**, 103666 (2022).

22. Bi, J., Zhao, Y., Wu, Z., Li, J. & Wang, C. Research on crack classification method and failure precursor index based on RA-AF value of brittle rock. *Theor. Appl. Fract. Mech.* **129**, 104179 (2024).

23. Wang, J. *et al.* Real-time identification of acoustic emission signals of rock tension-shear fracture based on machine learning and study on precursory characteristics. *Mech. Syst. Signal Process.* **230**, 112665 (2025).

24. Liu, J. *et al.* Acoustic emission evolution and fracture mechanism of rock for direct tensile failure. *Int. J. Rock Mech. Min. Sci.* **185**, 105974 (2025).

25. Feng, X. *et al.* Acoustic emission characteristics and cracking mechanism analysis of anisotropic shale containing a circular hole under uniaxial compression. *Theor. Appl. Fract. Mech.* **135**, 104771 (2025).

26. Wang, M. *et al.* Acoustic emission and fracture characteristics of red sandstone after high-temperature treatment. *Eng. Fract. Mech.* **306**, 110245 (2024).

27. Liu, X., Gong, B., Liang, Z., Zhang, Z. & You, X. Fracturing evolution of red sandstone: insights from three-point bending experiment and numerical simulation considering material inhomogeneity and internal discontinuities. *Bull. Eng. Geol. Environ.* **84**, 182 (2025).

28. Guo, J., Li, Y., Wang, Z., Chen, J. & Xu, C. Mechanical-acoustic-optical combined

565 characterization for uniaxial compression failure of soft-hard interbedded rock-like material. *J.*
566 *Mater. Res. Technol.* **39**, 4726–4744 (2025).
567 29. Chong, Z., Qiu, G., Li, X. & Yao, Q. Failure Law of Sandstone and Identification of
568 Premonitory Deterioration Information Based on Digital Image Correlation–Acoustic Emission
569 Multi-Source Information Fusion. *Appl. Sci.* **15**, 2506 (2025).
570 30. Hou, C., Li, X., Yin, T., Dong, L. & Sun, D. Experimental Investigation on Rock Failure
571 Characteristics of Large-Span Goafs Using Digital Image Correlation Analysis and Acoustic
572 Emission Monitoring. *Appl. Sci.* **14**, 9881 (2024).
573 31. Xie, P., Chen, W., Zhao, W. & Gao, H. Acquisition of acoustic emission precursor information
574 for rock masses with a single joint based on clustering-convolutional neural network method. *J.*
575 *Rock Mech. Geotech. Eng.* **16**, 5061–5076 (2024).
576 32. Yang, D., Chen, S., Liao, Z., Hu, B. & Xiao, S. Study on the acoustic emission and warning
577 information of layered limestone with fracture. *Eng. Fail. Anal.* **183**, 110224 (2026).
578 33. Karimpouli, S., Kwiatek, G., Martínez-Garzón, P., Dresen, G. & Bohnhoff, M. Unsupervised
579 clustering of catalogue-driven features for characterizing temporal evolution of labquake stress.
580 *Geophys. J. Int.* **237**, 755–771 (2024).
581 34. Matochkina, S. D., Shebalin, P. N., Smirnov, V. B., Ponomarev, A. V. & Malyutin, P. A.
582 Acoustic Emission Events Clustering Parameters in Laboratory Rock Fracture Experiments. *Izv.*
583 *Phys. Solid Earth* **60**, 913–922 (2024).
584 35. Zhang, Z., Wei, S. & Nan, H. Experimental Investigation on the Mechanisms of Fiber Bragg
585 Gratings to Monitor the Failure Processes of Pre-Cracked Sandstone Specimens. *Appl. Sci.* **15**,
586 12266 (2025).
587 36. Amitrano, D., Grasso, J. R. & Senfaute, G. Seismic precursory patterns before a cliff collapse
588 and critical point phenomena. *Geophys. Res. Lett.* **32**, L08314 (2005).
589 37. Senfaute, G., Duperret, A. & Lawrence, J. A. Micro-seismic precursory cracks prior to
590 rock-fall on coastal chalk cliffs: a case study at Mesnil-Val, Normandie, NW France. *Nat. Hazards*
591 *Earth Syst. Sci.* **9**, 1625–1641 (2009).
592 38. Occhiena, C., Pirulli, M. & Scavia, C. A microseismic-based procedure for the detection of
593 rock slope instabilities. *Int. J. Rock Mech. Min. Sci.* **69**, 67–79 (2014).
594 39. Feng, L., Intrieri, E., Pazzi, V., Gigli, G. & Tucci, G. A framework for temporal and spatial

595 rockfall early warning using micro-seismic monitoring. *Landslides* **18**, 1059–1070 (2021).
596 40. Torrence, C. & Compo, G. P. A Practical Guide to Wavelet Analysis. *Bull. Am. Meteorol. Soc.*
597 **79**, 61–78 (1998).
598
599